Scatter-limited conduction in printed platinum nanofilms

Goldie, D. M.; Hourd, A. C.; Harvie, M. R.; Thomson, J.; Abdolvand, A.

Published in:
Journal of Materials Science

DOI:
10.1007/s10853-014-8673-6

Publication date:
2015

Document Version
Peer reviewed version

First published in Journal of Material Science, Vol 50, Issue 3, February 2015 pages 1169 -1174.
The final publication is available at Springer via http://dx.doi.org/10.1007%2Fs10853-014-8673-6

Scatter-limited conduction in printed platinum nanofilms

D. M. Goldie * [1], A. C. Hourd [1], M. R. Harvie [2], J. Thomson [2] and A. Abdolvand [1]

[1] School of Engineering, Physics and Mathematics, University of Dundee, Dundee DD1 4HN, Scotland

[2] Ceimig Limited, Wester Gourdie Industrial Estate, Dundee DD2 4UT, Scotland

Abstract

It is demonstrated that thin platinum films may be deposited onto smooth glass substrates using a materials printer and a propriety organometallic ink. Under optimised printing and subsequent thermal curing conditions, excellent film adhesion to the substrates was achieved for thicknesses of about 15 nm. The resistivity of the optimised films is observed to be a factor of less than 3 higher than pure bulk platinum at 300 K and exhibits a slightly smaller associated thermal coefficient of resistance. The resistivity parameters are found to be insensitive to the gaseous measurement environment which suggests that intercalated carbon regions within the films following the curing process have been largely eliminated. An analysis of the resistivity data indicates that electronic conduction is consistent with enhanced boundary scattering at granular structures that are introduced during multi-pass printing. A minimum electron mean free path of ~ 18 nm is deduced from the measured film topography. The presented work will find application in biosensor and fuel cell technologies.

Keywords: platinum, printable materials, curing, scattering, resistivity

Introduction

The fabrication of low integration density electronic circuits and sensor systems using standard ink-jet printing technology [1,2] is becoming increasingly attractive in a number of commercial areas such as smart labelling and personal health-monitoring products. The active electronic inks that are deployed in such material printers range from insulators to metals and typically face a number of challenges to ensure that design features may be accurately reproduced whilst the electronic performance remains acceptable [3]. Popular metal inks generally comprise a suspension of nanoparticles which must be dried and sintered at high temperatures to achieve an acceptable resistivity for interconnect features [4-6]. These suspension inks frequently suffer from undesirable agglomeration effects which may lead to nozzle blocking and ultimately a limitation on the achievable resolution of printed features. Also, redistribution of the nanoparticulate material during coalescence and drying of the deposited ink droplets, the well documented "coffee-stain" effect [7-10], can be particularly troublesome for the preparation of high-quality, uniform films.

Alternative inks that offer to solve these printing limitations use solvated organometallic molecules [11-13]. Careful selection of the constituent organometallic molecule is vital, however, to ensure that the ensuing thermal curing process does not introduce intercalated carbon residues which limit the minimum achievable resistivity of the printed films. Significant effort has recently been reported on the development of printable gold inks [4-6,11] which have important applications as chemiresistor sensors and as electrode structures that possess a high chemical stability for lab-on-chip devices [14]. Compared to the advances made in the optimisation of gold inks relatively less progress has been reported for printed platinum (Pt) despite such films having potentially novel applications for biosensor and fuel cell technologies. Previous work using Pt organometallic inks has been largely focussed upon optimising the printing process but the achieved resistivity of the deposited films was found

to be much higher than pure bulk Pt [13]. The present work therefore investigates how the electrical performance of printed organometallic Pt films may be improved, and considers whether the measured resistivity behaviour is consistent with established thin-film electron scattering theories for the observed film morphology.

Materials and methods

To ensure that an acceptable performance of the inkjet materials printer (a Fujifilm Dimatix DMP-2801) was achieved, considerable effort was taken to optimise the surface tension and viscosity of the printable Pt fluid. The selected Pt ink formulation, supplied by Ceimig Limited, comprised a 3-component solvent system (toluene, cyclopentanone and cyclohexanol in various ratios) into which a Pt organometallic, dimethyl(1,5-cyclooctadiene)platinum(II), was dissolved. Surface tension measurements on these inks were made using a Krüss EasyDrop drop shape analysis system, whereby the shape of a pendant drop of the ink solution is suspended in air and its shape captured and modelled by the system to yield the surface tension. The dynamic viscosity of the inks was measured using a Cannon-Fenske viscometer tube, immersed in a constant temperature bath. Using these measurement procedures, the ratios of the 3-component solvent system making up the ink formulation were adjusted to produce an optimal printing performance in the printer (surface tension = 31.3 ± 0.6 mNm^{-1}; dynamic viscosity = 16.6 ± 0.5 cP at 21 °C).

For resistivity measurements serpentine track patterns (1 mm wide and 50 mm long) were printed onto microscope glass substrates which had been ultrasonically pre-cleaned in acetone. Surface priming of the cleaned glass substrates (using hexamethyldisilazane vapour) did not improve the overall print quality. The printer platen and ink cartridge temperatures were maintained at 30 ^{o}C during the printing period. The voltage waveforms used to drive the print-head resulted in an approximated drop velocity of 7.5 ms^{-1} and a drop overlap distance of 20 μm. A 4-jet (or greater) delivery method from a print height of 0.75 mm was found to

be beneficial for overall uniformity of the material distribution in the printed serpentine track patterns. For multi-pass printing of patterns a delay of 60 s was imposed between printing each layer.

Curing of the printed ink patterns to produce corresponding Pt metal features was performed by thermally annealing the substrates at a temperature of 320 ^{o}C for 300 s in an air ambient. The thickness of the cured films was established using a surface profilimeter, and the surface topography imaged using an atomic force microscope (AFM). The electrical resistivity of the cured films was measured using a computer controlled source-measure system (Keithley model 236) by sweeping a source voltage between 0.1 V to 1.0 V across the length of the serpentine track and monitoring the induced current flow. Resistivity measurements were conducted between 170 K and 400 K by mounting the printed samples in a liquid nitrogen bath cryostat (Oxford Instruments Optistat DN). Various dry thermal exchange gases (helium, nitrogen and argon at a pressure of about 1 atmosphere) were used during cryostat operation.

Results and discussion

The quality of the graphical patterns that could be reproduced using the Pt ink formulation under optimised printing conditions is illustrated in Fig. 1(a). This serpentine track pattern shows excellent edge acuity and minimal corner rounding following the curing stage. The distribution of deposited ink across the printed pattern is correspondingly very uniform which indicates that the adopted ink formulation promotes stability of the droplets in flight whilst allowing unwanted trailing satellite droplets to be controlled. The quality of these Pt patterns is comparable to independent work using similar Pt organometallic inks [13].

The average film thickness (d_{avg}) and associated surface roughness (h) were determined for structures such as shown in Fig. 1(a). Data for d_{avg} and h were obtained either for very thin

film structures that were deposited using only a single-pass print, or on thicker films which involved successive over-printing of the structure using a multi n-pass scheme ($2 \leq n \leq 4$). Due to the sensitivity of the profilimeter equipment, reliable thickness measurements could only be obtained for the multi-pass films and for $n = 3$ a value of $d_{avg} = 15 \pm 5$ nm was obtained. The necessity of using multi-pass printing to obtain sufficiently thick films for profilimetry scanning was accompanied, however, by corresponding changes to the overall film morphology. Significant differences in the surface topology between the single-pass and multi-pass films were revealed in Fig. 1. Single pass films (Fig. 1(b)) were universally found to exhibit a very smooth surface ($h < 1$ nm) whereas for the multi-pass films (Fig. 1(c); $n = 4$) the surface is found to be considerably rougher (2 nm $< h <$ 8 nm) and comprises a granular structure with an associated spatial diameter of around 60 nm. Multi-pass printing does not therefore simply result in thicker films as the behaviour of the ink drying and curing processes are expected to be different according to the wetting characteristics and droplet interaction of the printed receptor surface. The granular structure that is observed in Fig.1(c) is not consistent with the known droplet spacing distances but probably results from larger precursor granules that form during the repeated solvation / drying cycles associated with multi-pass printing. These then become manifest as larger Pt granules after curing so that a multi-pass film most likely comprises the observed granular structure which grows out of a thin single-pass film of Pt. Evidence to support this multi-pass morphology is provided by so-called "Scotch-tape" adhesion tests [15]. Films for $n \leq 3$ were generally found to pass the adhesion test comfortably, but for $n > 3$ there were sometimes signs of delamination of the upper part of the film although a thin underlying Pt layer was always found to adhere to the glass substrate.

The electrical performance of single-pass Pt films was often observed to be inconsistent due to suspected discontinuities along the relatively long length (50 mm) of the serpentine test

pattern. Resistivity testing of the printed Pt was consequently concentrated upon multi-pass (n = 3) films where consistent resistance values (880 ± 78 Ω at 300 K) were obtained for a number of identically prepared serpentine structures. The deduced resistivity (ρ) of these films (using d_{avg} = 15nm) are given as a function of temperature (T) in Fig. 2. Compared with the reference $\rho(T)$ data shown for pure bulk Pt [16] the printed n = 3 films are seen to possess slightly higher resistivity values and an associated weaker thermal dependence. The resistivity of these films is considerably closer to bulk Pt than previously reported data using organometallic Pt inks (ρ(300 K) ~ 4 x 10^{-2} Ωm [13]). The significant improvement strongly suggests that the present films do not suffer from the inclusion of intercalated carbon residues that may result from incomplete removal of the organic carrier during the curing process. The printed films are accordingly expected to be non-porous and this is confirmed in Fig. 2 by the relative insensitivity of the $\rho(T)$ data to the use of different thermal exchange gases within the cryostat. A small systematic trend is evident with the resistivity increasing as relative permittivity of the ambient gas decreases. This indicates that the gas is able to penetrate the cured Pt structure to some degree although from the magnitude of the resistivity changes conduction is obviously still dominated by a continuous metallic network. Such a level of gas penetration is of potential use for sensor and electrochemical device applications.

The $\rho(T)$ behaviour displayed in Fig. 2 for the printed Pt films is similarly observed in nanometre-thick Pt films that are deposited using either thermal [17] or electron beam [18] evaporation techniques. For these Pt thin films the characteristic resistivity behaviour is attributed to enhanced scattering at either the film surface and / or at crystallite grain boundaries. By performing in-situ resistivity measurements during film growth it has been demonstrated that the individual effects of surface and grain boundary scattering may be separated [17] by applying the scattering theories of Fuchs [19] and Namba [20] for films

whose one-dimensional spatial thickness dependence $d(x)$ is modelled as a sinusoidal fluctuation of wavelength s such that

$$d(x) = d_{avg} + h\sin\left(\frac{2\pi x}{s}\right) \tag{1}$$

Both the mean resistivity $\rho(d_{avg})$, and the associated mean temperature coefficient of resistivity $\beta(d_{avg})$, may then be obtained by averaging the local conductivity $\sigma(d(x))$ and temperature coefficient of resistivity $\beta(d(x))$ along the full length (L) of the film which lies parallel to the current. The ensuing expressions for $\rho(d_{avg})$ and $\beta(d_{avg})$ relative to the corresponding bulk quantities ρ_b and β_b in the absence of scattering are given by [17]

$$\frac{\rho(d_{avg})}{\rho_b} = \frac{d_{avg}}{L}\int_0^L \frac{\rho_b^{-1}}{\sigma(d(x))d(x)}dx \tag{2}$$

$$\frac{\beta(d_{avg})}{\beta_b} = \frac{1}{L}\int_0^L \beta(d(x))dx \tag{3}$$

In Eq. (2) $\sigma(d(x))$ is given by the Fuch's integral [19] and depends upon the fraction (p) of electrons that are elastically scattered from the film surface and the electron mean free path (l_0). By contrast the $\beta(d(x))$ quantity that appears in Eq. (3) is only sensitive to the mean free path [18, 21]. A comparison of the magnitudes of both $\rho(d_{avg})$ and $\beta(d_{avg})$ for the printed Pt films relative to the bulk Pt values should consequently permit information about p and l_0 to be deduced provided that accurate knowledge of the film topography parameters (d_{avg}, h and s) is available. Values for d_{avg} and h for the n = 3 printed films have already been noted, and an initial estimate of s = 60 nm is suggested by the AFM imaging (Fig 1c).

An evaluation of the Fuchs-Namba scattering model using Eq. (3) and Eq. (4) may then proceed by setting L = 50 mm for the serpentine track length. Because experimental data is presently only available for a single value of d_{avg} associated with the n = 3 printing procedure, it is important to appreciate that analysis by the Fuchs-Namba equations will only allow an assessment of whether purely surface scattering effects can account for the observed $\rho(T)$ behaviour. Under these circumstances the value of d_{avg} that is used for the printed films can have a significant influence upon the experimentally calculated magnitude for $\rho(d_{avg})$ from the measured resistance and hence the deduced fitting parameters (p and l_0) from Eq. (3). Since $\beta(d_{avg})$ is independent of d_{avg}, the preferred fitting strategy is thus to initially obtain estimates for l_0 via Eq. (3) and to subsequently use these l_0 estimates in Eq. (2) to determine the corresponding solutions for p. The results generated by this fitting procedure are summarised in Fig. 3 where the resistivity data for the He atmosphere in Fig. 2 have been used at a reference temperature of T = 300 K . The calculated solutions for l_0 and p were found to be completely insensitive to the value of s used in Eq. (1) provided $(s / L) \ll 1$. Both the l_0 and p parameters depend upon the ratio of h / d_{avg} and are given parametrically over a range of d_{avg} values that reflects the experimental uncertainty that is associated with the thickness measurements of the n = 3 films. The mean free path is found to scale linearly with d_{avg} as confirmed in Fig. 3a, and for $(h / d_{avg}) < 0.5$ the mean free path for the printed films requires that $l_0 > 5 \times d_{avg}$. The corresponding p values to account for $\rho(d_{avg})$ are plotted in Fig. 3b where it is evident that physically acceptable solutions ($p \leq 1$) demand that the film surface is not abnormally rough ($h / d_{avg} < 0.7$). Using the mean experimental values for d_{avg} = 15 nm and h = 5 nm, Fig. 3 returns values for l_0 = 78 nm and p = 0.46. The deduced mean free path is much longer than that found in pure bulk Pt (23 nm [17,18]), whilst the high value for p is inconsistent with the rough surface topology of the n = 3 films. A fit using the upper limit of 23 nm for l_0 would require that $d_{avg} < 5$ nm from Fig. 3b but for such film

thicknesses, which lie significantly out with the experimental limits, the associated p magnitudes are greater than unity across the entire range of (h / d_{avg}) values. Surface scattering effects alone do not therefore appear to be capable of accounting for the experimentally observed $\rho(T)$ behaviour of the printed Pt films.

An alternative scattering mechanism which may exist in the printed Pt films is provided through the presence of internal grain boundaries. Such boundaries may arise from the granular morphology detected by AFM imaging on multi-pass films if the grains extend throughout a significant fraction of the film thickness. Grain-boundary scattering has been shown to be the dominant scattering process in Pt films deposited by e-beam evaporation [18] and is also inferred for thermally evaporated Pt films where surface scattering is also present [17]. For metallic films that possess a polycrystalline morphology, electron scattering at the inter-crystallite grain boundaries has been interpreted using the Mayadas and Shatzkes theory [22,23] which predicts the increased resistivity in terms of a dimensionless parameter α that involves the carrier mean free path l_0, the average crystallite diameter (D) and the reflection coefficient (R) for elastic scattering where;

$$\alpha = \left(\frac{l_0}{D}\right)\left(\frac{R}{1-R}\right) \tag{4}$$

The associated decrease in the temperature coefficient of resistivity is also dependent upon α [24] so that for pure grain boundary scattering where surface scattering is absent ($p = 0$) the overall $\rho(T)$ behaviour should be expressible by a common value for α. The expressions for $\rho(\alpha)$ and $\beta(\alpha)$ relative to the corresponding bulk quantities ρ_b and β_b in the absence of scattering are then most compactly expressed as

$$\frac{\rho(\alpha)}{\rho_b} = \left(1 - \frac{3}{2}\alpha + 3\alpha^2 - 3\alpha^2 \ln\left(1 + \frac{1}{\alpha}\right)\right)^{-1} \tag{5}$$

$$\frac{\beta(\alpha)}{\beta_b} = 1 + \frac{\rho(\alpha)}{\rho_b}\left[-\frac{3}{2}\alpha + 6\alpha^2 + \frac{3\alpha^3}{1+\alpha} - 9\alpha^3 \ln\left(1+\frac{1}{\alpha}\right)\right] \quad (6)$$

Applying the Mayadas and Shatzkes theory to the n = 3 printed Pt data it is thus possible to estimate (l_0 / D), for appropriate values of R, over the relevant experimental range of d_{avg} film thicknesses. The results from this fitting procedure are given in Fig. 4 where it is found that the optimum fit for both $\rho(\alpha)$ / ρ_b and $\beta(\alpha)$ / β_b occurs when d_{avg} ~ 17 nm which is consistent with the experimental film thickness measurements. The associated value of α for this thickness is 1.14 so that, setting 0.6 < R < 0.8 as deduced from other polycrystalline thin Pt films [17,18], it is deduced from Eq. 4 that 0.3 < (l_0 / D) < 0.8, which would be the case if grain boundary scattering is solely responsible for the observed $\rho(T)$ behaviour of the printed films. If the crystallite diameter D is identified with the granular size of 60 nm measured in AFM images (Fig. 1c) the corresponding range for the mean free path is then calculated as 18 nm ≤ l_0 ≤ 48 nm. The lower limit of this range is physically acceptable compared with the mean free path for bulk Pt and is only slightly higher than that found for evaporated Pt thin films (11 nm [17]). A reduced mean free path in the present printed Pt films may be indicative of additional internal-grain scattering at small organometallic impurities that are not removed during curing.

Scattering by grain-boundaries would therefore appear to explain the resistivity differences that exist between the printed Pt films and pure bulk Pt using parameters that are consistent with the measured film morphology. However, it is important to appreciate that the required scattering at such grain-boundaries is relatively weak since the number of boundaries that are crossed in a mean free path (= l_0 / D) is less than unity. The influence of grain-boundary scattering may even be weaker as the Mayadas and Shatzkes theory ignores surface scattering effects. If it were possible to print smooth (h = 0) Pt films with no underlying granular

structure ($D \rightarrow \infty$, $\alpha = 0$), only surface scattering will limit the achievable resistivity as the film thickness become comparable to the mean free path. Using the minimum value of l_0 = 18 nm deduced above the corresponding minimum $\rho(d_{avg}) / \rho_b$ ratio that is estimated from Eq. 2 is 1.5 at 300 K for d_{avg} = 17 nm. The granular structure that is introduced during multi-pass printing thus introduces an unwanted (2.3 / 1.5) factor increase in the printed film resistivity. Interestingly, it is estimated that for the thinner single-pass films, assuming $d_{avg} \sim$ (17 / 3) nm, $\rho(d_{avg}) / \rho_b$ = 2.4 at 300 K. Thus, even if it were possible to print such films that were electrically continuous, the resistivity is expected to be very similar to that measured for the n = 3 multi-pass films as surface scattering would be enhanced in these thinner films.

Conclusions

Organometallic inks provide a realistic option for the deposition of thin film Pt structures using inkjet printing techniques that are comparable in quality to thin Pt films prepared by conventional thermal evaporation techniques. Films printed onto glass substrates display good adhesion properties and appear to be devoid of any intercalated carbon regions following a simple thermal curing process to produce Pt metal features. The slightly higher resistivity of multi-pass printed films compared to pure bulk Pt is consistent with grain-boundary scattering effects associated with granular structures that are introduced during multi-pass printing. The potential ability to print smoother multi-pass films through advances in the ink and associated printing procedure is anticipated to further reduce the resistivity.

References

1. Sirringhaus H, Kawase T, Friend, RH et al (2000) High resolution inkjet printing of all-polymer transistor circuits. Science 290: 2123-2126
2. Singh M, Haverinen, HM, Dhagat, P and Jabbour, GE (2010) Inkjet printing-process and its applications. Adv Mat 22:673-685
3. Cummins G and Desmulliez MPY (2012) Inkjet printing of conductive materials: a review. Circuit World 38:193-213
4. Raguse, B, Chow, E, Barton, CS and Wieczorek, L (2007) Gold nanoparticle chemiresistor sensors: direct sensing of organics in aqueous electrolyte solution. Analyt Chem 79: 7333-7339
5. Chow, E, Herrmann, J, Barton, CS, Raguse, B and Wieczorek, L (2009) Inkjet-printed gold nanoparticle chemiresistors: influence of film morphology and ionic strength on the detection of organics dissolved in aqueous solution. Analyt Chimica Acta 632: 135-142
6. Cooper, JS, Raguse, B, Chow, E et al (2010) Gold nanoparticle chemiresistor sensor array that differentiates between hydrocarbon fuels dissolved in artificial seawater. Analyt Chem 82: 3788-3795
7. Deegan, RD, Bakajin, O, Dupont, TF, Huber, G, Nagel, SR, and Witten, TA (1997) Capillary flow as the cause of ring stains from dried liquid drops. Nature 389: 827-829
8. Deegan, RD, Bakajin, O, Dupont, TF, Huber, G, Nagel, SR, and Witten, TA (2000) Contact line deposits in an evaporating drop. Phys Rev E 62: 756-765
9. Routh, AF and Zimmerman, WB (2004) Distribution of particles during solvent evaporation from films. Chem Eng Sci 59: 2961-2964
10. Park, J and Moon, J (2006) Control of colloidal particle deposit patterns within picoliter droplets ejected by ink-jet printing. Langmuir 22: 3506-3513

11. Nur, HM, Song, JH, Evans, JRG and Edirisinghe, MJ (2002) Ink-jet printing of gold conductive tracks. J Mat Sci: Mat in Elect 13: 213-219
12. Smith, PJ, Shin, DY, Stringer, J, Derby, B and Reis, N (2006) Direct ink-jet printing and low temperature conversion of conductive silver patterns. J Mat Sci 41: 4153-4158
13. Cummins G, Kay R, Terry J et al (2011) Optimization and characterization of drop-on-demand inkjet printing process for platinum organometallic inks. 13th Electronics Packaging Technology Conference: 978-1-4577-1982-0/11 IEEE, pp 256-261
14. Ghafhar-Zade, E, Sawan M (2010) CMOS Capacitive Sensors for Lab-on-Chip Applications: A Multidisciplinary Approach. Springer, New York
15. Mittal KL (1976) Adhesion measurement of thin films. Electro Sci and Tech 3:21-42
16. Corti CW (1984) Thermophysical data on platinum: resistivity and conductivity values recommended. Plat Met Rev 28:164-165
17. Vancea J, Horst H and Kastner K (1984) Mean free path and effective density of conduction electrons in polycrystalline metal films. Thin Solid Films 121:201-216
18. Zhang QG, Zhang X, Cao BY et al (2006) Influence of grain boundary scattering on the electrical properties of platinum nanofilms. Appl Phys Lett 89:11402 1-3
19. Fuchs K (1938) The conductivity of thin metallic films according to the electron theory of metals. Proc Cambridge Philos Soc 34:100-108
20. Namba Y (1970) Resistivity and temperature coefficient of thin metal films with rough surface. Jpn J Appl Phys 9:1326-1329
21. Tellier CR, Tosser AJ and Boutrit C (1977) Mayadas-Shatzkes conduction model treated as a Fuchs-Sondheimer model. Thin Solid Films 44:201-208

22. Mayadas AF, Shatzkes M and Janak JF (1969) Electrical resistivity model for polycrystalline films -case of specular reflection at external surfaces. Appl Phys Lett 14:345-347
23. Mayadas AF and Shatzkes M (1970) Electrical-resistivity model for polycrystalline films -case of arbitrary reflection at external surfaces. Phys Rev B 1:1382-1389
24. Tellier CR and Tosser AJ (1977) Temperature-coefficient of resistivity of polycrystalline radio-frequency sputtered aluminium films. Thin Solid Films 43:261-266

Acknowledgements

This work was conducted under the aegis of the Scottish Universities Physics Alliance (SUPA) Industrial Placement Scheme and the Engineering and Physical Sciences Research Council (EPSRC) of the United Kingdom (EP/I004173/1). The assistance of Dr Y. Fan with the acquisition and interpretation of the AFM data is gratefully acknowledged. Amin Abdolvand is an EPSRC Career Acceleration Fellow at the University of Dundee.

Figure Captions

Fig.1 Printed Pt film images (a) multi-pass n = 3 serpentine track pattern; nominal line width = 1 mm (b) single pass AFM image showing very smooth surface (b) n = 4 multi- pass AFM image showing granular structure

Fig. 2 Temperature dependence of the resistivity for n = 3 multi-pass printed Pt films using an average film thickness of 15nm. The solid line shows the best linear fit to data recorded in a He atmosphere. The dashed curve is for pure bulk Pt [16]

Fig. 3

(a**)** Calculated mean-free-path as a function of relative surface roughness using Eq. (3)

(b) Calculated spectral probability as a function of relative surface roughness for various film thickness using Eq. (2)

Fig. 4 Mayadas-Shatzkes fit to the resistivity ratio, and the temperature coefficient of resistivity ratio, for printed relative to pure bulk Pt as a function of average film thickness

Figure 1

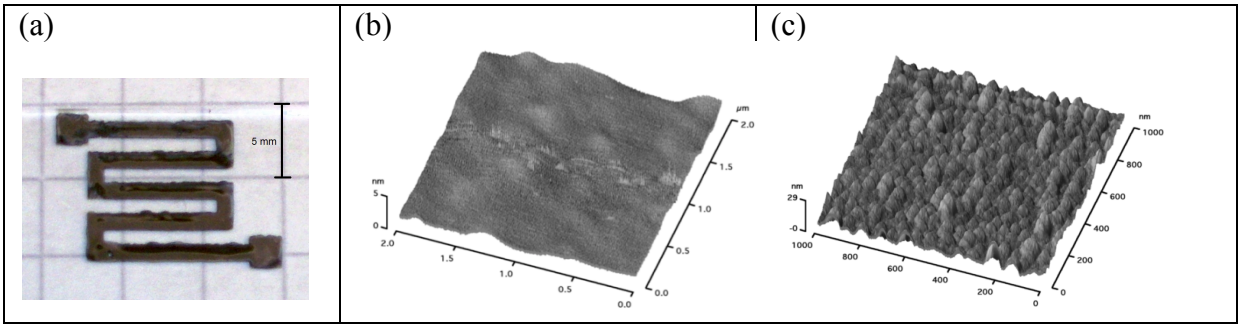
(a)
5 mm
(b)
nm
5
0
2.0
1.5
1.0
0.5
0.0
µm
2.0
1.5
1.0
0.5
0.0
(c)
nm
29
-0
1000
800
600
400
200
0
nm
1000
800
600
400
200
0

Figure 2

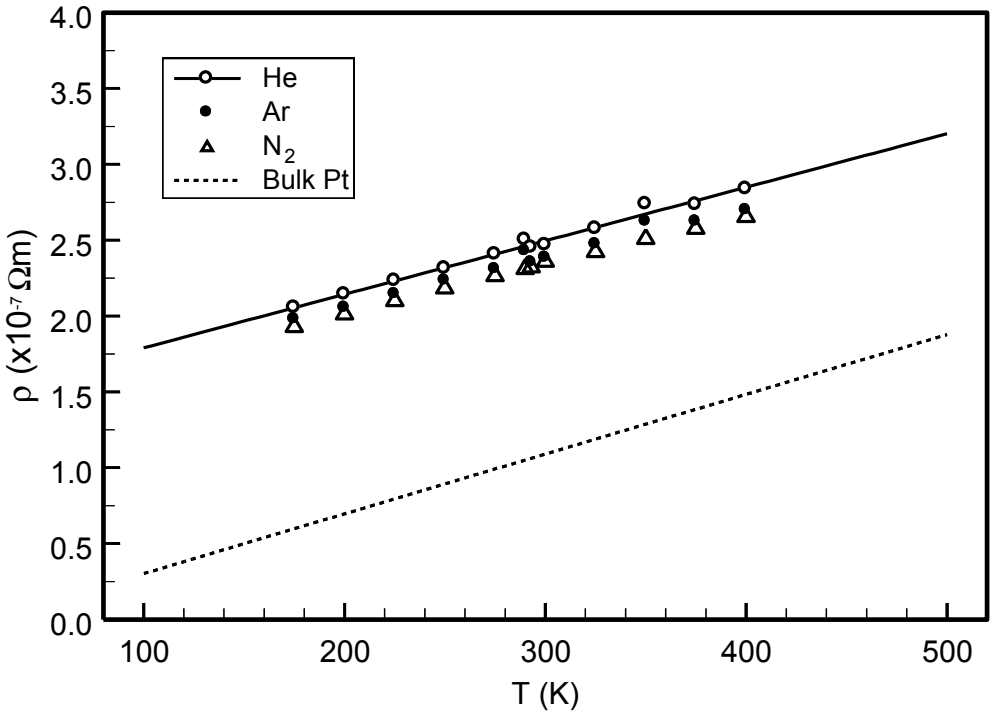
4.0
3.5
3.0
2.5
2.0
1.5
1.0
0.5
0.0
ρ (x10-7 Ωm)
100
200
300
400
500
T (K)
He
Ar
N2
Bulk Pt

Figure 3

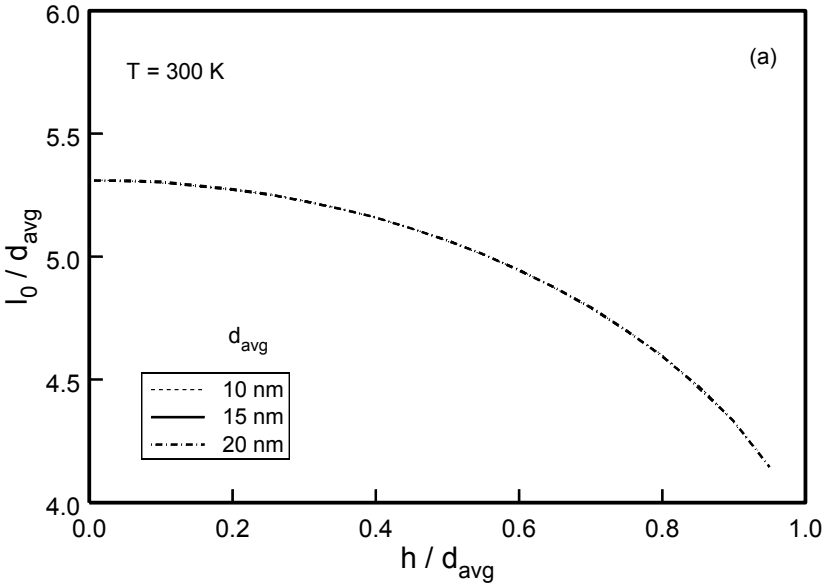
T = 300 K
(a)
l_0 / d_{avg}
h / d_{avg}
d_{avg}
10 nm
15 nm
20 nm

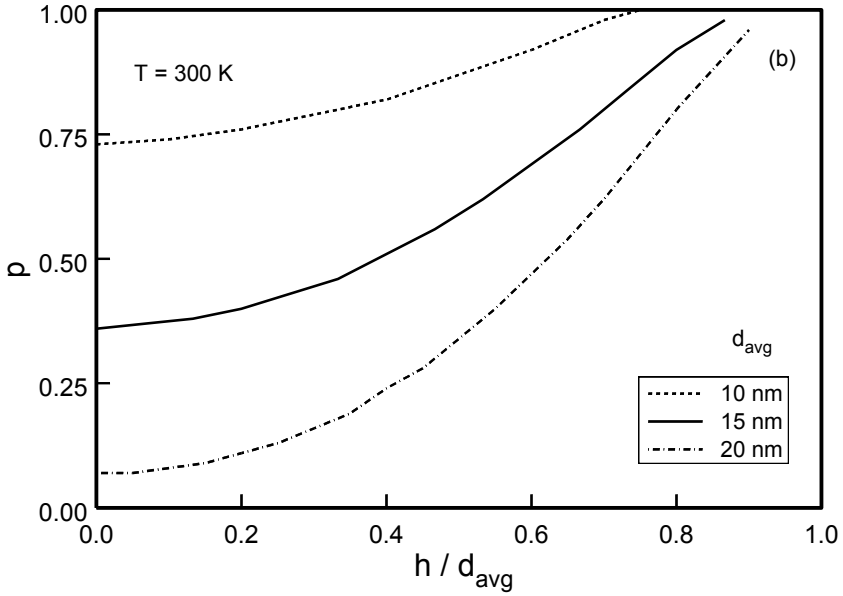
T = 300 K
(b)
p
h / d_{avg}
d_{avg}
10 nm
15 nm
20 nm

Figure 4

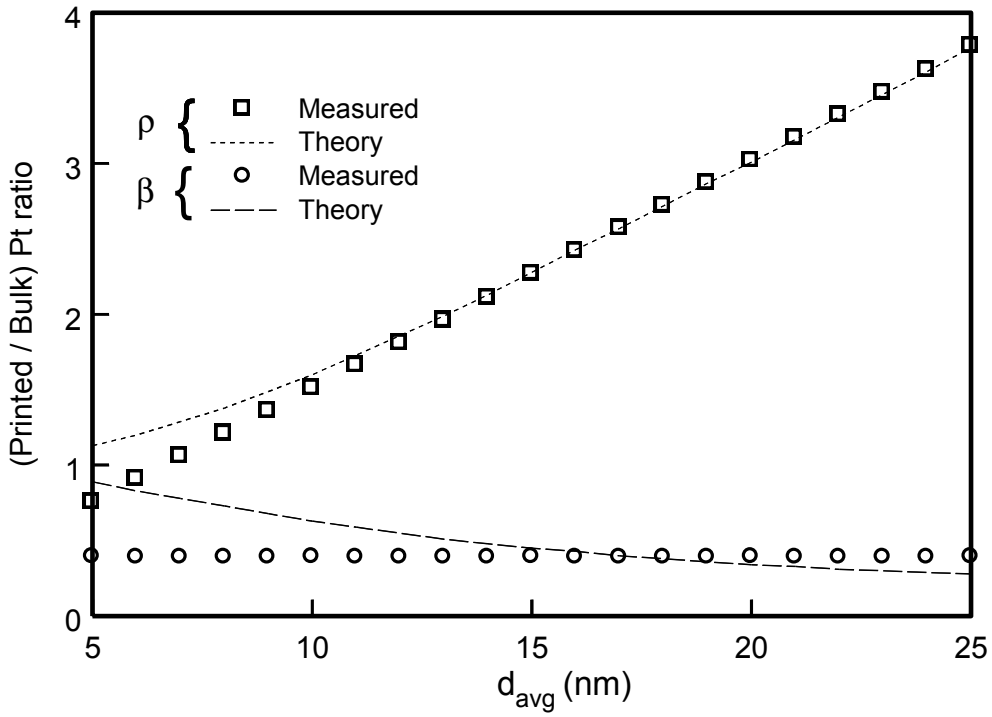
(Printed / Bulk) Pt ratio
4
3
2
1
0
5
10
15
20
25
d_{avg} (nm)
ρ
Measured
Theory
β
Measured
Theory